View metadata, citation and similar papers at core.ac.uk

brought to you by CORE

provided by KITopen

Batteries & Supercaps | doi.org/10.1002/batt.202000178

European Chemical Societies Publishing

Heterogeneity of Graphite Lithiation in State-of-the-Art Cylinder-Type Li-Ion Cells

Dominik Petz,[a, b] Martin J. Mühlbauer,[a, c, d] Alexander Schökel,[a, d, e] Klaus Achterhold,[f] Franz Pfeiffer,[f, g] Thilo Pirling,[h] Michael Hofmann,[a] and Anatoliy Senyshyn*[a]

The two-dimensional lithium distribution in the graphite anode was non-destructively probed by spatially resolved neutron diffraction for a batch consisting of 34 different cylinder-type (18650) Li-ion batteries in fully charged state. The uniformity of the lithium distribution was quantified and correlated to the cell specifications/electrochemistry and to intrinsic cell parameters like electrode thickness, position of current collectors, etc. which were obtained by X-ray micro-computed tomography. Non-uniformities in the lithiation state of the anode from a constant plateau have been observed for the majority of the studied cells. Their location corresponds to the positions of current tabs connecting the electrode stripes and areas of incomplete electrode coating at the beginning and the end of the electrode stripes. Four commonly used schemes of current lid connection were identified. Each of them displays its own effect on the uniformity of the lithiation at the anode and, therefore, variation of the intrinsic state-of-charge distribution and, most probably, the ageing behavior of the electrodes.

1. Introduction

Energy storage media based on Li-ion technology are peaking in their popularity for power and energy supply and implemented/embedded in wearable and portable electronics, cordless and communication tools and/or electric drivetrains. Such a broad range of applications for Li-ion batteries and their day-to-day use bring lifetime, cycling stability and safety issues to the same level of significance as energy and power density.[1–3] It is well known that lithium ion batteries lose part of their capacity upon cycling and due to calendar aging, which involves different fading mechanisms, e.g. loss of movable lithium, electrolyte decomposition and degradation of active electrode material, which is supplemented by an increased internal resistance of the cell, thus reducing efficiency.[4,5] It is worth to note that the majority of fading mechanisms accompanying standard cell operation are heterogeneous in their nature.[6,7] This can be illustrated by a simple consideration: for example, the rate of reactions occurring in lithium-ion batteries are highly temperature dependent;[8] cell charge/discharge (as a source of non-uniform current density distribution)[9–12] produces temperature gradients in different cell parts,[13] leading to different reaction rates, and by this, to a difference in fading. The heterogeneous character of cell operation leads to a non-uniform lithium-ion distribution inside the cell,[14,15] which affects the cell performance, lifetime and safety.

The use of battery modules equipped with thermal management systems further adds to the complexity of predicting and describing the reaction mechanisms. Furthermore, in order to reach an optimum volumetric energy density, modern lithium-ion cells are manufactured in various shapes. A clear trend towards an increase of capacity on the single cell level can be observed, where issue of cell uniformity and relevant tools for its studies gain in importance. Lithium-ion

[a] D. Petz, Dr. M. J. Mühlbauer, Dr. A. Schökel, Dr. M. Hofmann, Dr. A. Senyshyn
Heinz Maier-Leibnitz Zentrum (MLZ)
Technische Universität München
Lichtenbergstr. 1, 85748 Garching, Germany
E-mail: anatoliy.senyshyn@gmail.com
[b] D. Petz
Lehrstuhl für funktionelle Materialien, E13
Technische Universität München
James-Franck-Str. 1/I, 85748 Garching b. München, Germany
[c] Dr. M. J. Mühlbauer
Helmholtz-Institute Ulm for Electrochemical Energy Storage (HIU)
Karlsruhe Institute of Technology (KIT)
P.O. Box 3640, D-76021 Karlsruhe, Germany
[d] Dr. M. J. Mühlbauer, Dr. A. Schökel
Institute for Applied Materials (IAM)
Karlsruhe Institute of Technology (KIT)
Hermann-von-Helmholtz-Platz 1,
76344 Eggenstein-Leopoldshafen, Germany
[e] Dr. A. Schökel
Deutsches Elektronen Synchrotron (DESY)
Notkestr. 85, 22607 Hamburg, Germany
[f] Dr. K. Achterhold, Prof. F. Pfeiffer
Department of Physics & Munich School of Bioengineering
Technische Universität München
James-Franck-Straße 1, 85748 Garching, Germany
[g] Prof. F. Pfeiffer
Department of Diagnostic and Interventional Radiology
Munich School of Medicine and Klinikum rechts der Isar
Ismaninger Str. 22, 81675 Munich, Germany
[h] Dr. T. Pirling
Institut Max von Laue – Paul Langevin (ILL)
71, Avenue des Martyrs,
38043 Grenoble Cedex 9, France

Supporting information for this article is available on the WWW under https://doi.org/10.1002/batt.202000178

© 2020 The Authors. Batteries & Supercaps published by Wiley-VCH GmbH. This is an open access article under the terms of the Creative Commons Attribution License, which permits use, distribution and reproduction in any medium, provided the original work is properly cited.

batteries are closed electrochemical systems, which can easily be driven out of their thermodynamic equilibrium and change their state upon opening (by, e.g., redox reactions of electrode material, evaporation of the electrolyte, change of mechanical pressure, modified wetting conditions and electrical contacts of the electrodes and so on). Therefore, battery R&D requires non-destructive experimental techniques capable to deliver information under real operating conditions. As such, an *in situ* technique capable to unambiguously determine the lithiation grade of the electrodes without cell disassembly is desirable. Another important aspect is that the technique should be capable to deliver depth information in order to probe its spatial distribution. Among the variety of non-destructive techniques, neutron scattering (especially diffraction) is particularly suited due to numerous advantages:

- Neutrons are weakly interacting with matter in general, which leads to high achievable penetration depth and, thus, enables studies of bulky samples or objects in complex environments.
- The wavelength of thermal neutrons is comparable to interplanar spacings in crystal structure, enabling accurate neutron diffraction studies. The atomic form factor is independent from $\sin(\Theta)/\lambda$ because of the interaction with the nuclei, which results in accurate structure factors and, correspondingly, high quality structural data.
- Neutrons are not only isotope-sensitive, but also show large variation of scattering length, i.e. light elements can be localized next to heavy ones because of their distinctly different scattering cross sections. Therefore, neutron diffraction displays an enhanced sensitivity to light atoms (including lithium) and to transition metals making it complementary to X-ray diffraction, scattering and absorption. An isotope contrast can further improve the sensitivity and localization power, e.g., using isotope markers.

Neutron scattering is actively explored in battery research and, indeed, neutron diffraction is one of the most commonly used technique in the field. It offers a non-destructive way to assess the lithiation degree of anode and cathode, which is reflected by the response of the crystal structures on the momentary state-of-charge (SOC)[16] and state-of-health (SOH).[17] Such kind of *in situ* neutron diffraction studies are performed on Li-ion cells of different designs, either laboratory[18–21] or commercial[22–24] type. In recent years a number of neutron diffraction studies dedicated to the lithiation of either positive or negative electrode materials,[25–31] aging behavior[32,33] and effects of temperature.[34,35]

The majority of the above-mentioned reports focuses on the structure evolution obtained by integration over a large cell volume, assuming the studied cells to be uniform. Literature on the experimental studies of lithium uniformity on the cell level is quite limited: Cai et al.[36] reported a non-uniform degradation in large format pouch bag cells using time-of-flight neutron diffraction as a local probe; Yu et al.[37] proposed an approach for simultaneous studies of local temperature, SOC and strain. A method for probing the 2D lithium distribution in the graphite anode using monochromatic neutron diffraction (alternative to time-of-flight neutron diffraction) was proposed in literature.[38] The method was successfully applied to monitor the lithium distribution in four 18650-type cells adopting different configurations of current tabs[14] and to probe the lithium distribution in variously fatigued high energy lithium cobalt oxide LCO|C[39] and high performance lithium nickel cobalt aluminum Oxide NCA|C[32] cells. Recently, an attempt to localize and quantify the electrolyte in frozen state was made by a similar experimental approach at low temperatures.[33] The lithium distribution has been found strongly affected by the configuration of the current tabs and by the cell SOH leading to an increasingly heterogeneous character of cell fatigue. Besides neutron diffraction there is a number of neutron-based scattering and spectroscopic techniques capable to localize lithium (e.g., neutron depth profiling,[40] neutron imaging,[24] neutron reflectometry[41] and small/wide angle neutron scattering,[42] etc.), where neutron diffraction seems to be the optimal solution for non-destructive studies of assembled cell and spatial resolution on mm scale.

Therefore, previous studies[14] were extended to a larger batch of cylinder cells of different type. The aim of the current work is to establish a correlation between the experimentally determined spatial distribution of lithium×in lithiated graphites Li_xC_6, the electrochemical performance of the cell, i.e. its capacity and/or nominal currents as well as details of the inner cell organization and morphology like electrode thickness, position of current tabs, etc. In the frame of the current study a batch consisting of 34 different cells was investigated, where their cylinder type (18650) shape, rolled electrode stacks and graphite anode were common criteria for the cell selection.

Experimental Section

Galvanostatic cell cycling

The batch of 18650-type Li-ion secondary cells was composed of various types produced by different manufacturers. Their electrochemical characterization was carried out using a Neware BTS4000 multichannel potentiostat applying constant current (CC) discharge and constant current constant voltage (CCCV) charge protocols. For sake of comparison to previous data and to minimize the effects driven by relaxations and drifts on the cell parameters, the applied current in the CC part of charging/discharging was set to 400 mA and the cut-off current in CV region was set to 1% of the nominal 1 C current (different for each cell type). Cell-specific voltage windows were applied, where the lower and upper voltage boundaries were taken from the nominal voltage values provided by the cell manufacturers. An overview of the cycling parameters is given in Table 1.

X-ray computed tomography

A high-resolution phoenix v|tome|x 240s system was utilized for characterization of the cells by X-ray micro-computed tomography (X-Ray microCT). The acceleration voltage was set to 130 kV and the current to 100 μA either using direct or transmission tube. Data collection was performed using a CCD detector, DXR-250RT General Electric, with a CsI scintillator of 700 mm thickness, an active area of 1000×1000 pixels and a pixel size of 200 μm×200 μm. For each cell 1001 projections (X-ray radiography images) were produced

© 2020 The Authors. Batteries & Supercaps published by Wiley-VCH GmbH

Table 1. Summarized list of parameters and obtained characteristics of studied 18650-type cells.

Nr	Manufacturer	Cell type	Capacity [mAh]		Current[a] [A]		Voltage	Tab	Current tab [cm]			Thickness[b]	Concentration × in Li_xC_6			Parameters plateau			C[c] excess
			nominal	observed	charge	discharge	[V]	scheme	"+"	"−"	"− "	[μm]	plateau	median	mean	η	x_c	w	
1	Samsung	INR 18650 20R[d]	2000	1905.2	4	22	2.5–4.2	3	5.32	3.06	5.24	253	0.839	0.826	0.812	0.660	0.839	0.027	1.267
2	Samsung	ICR 18650 30 A	3000	2694.1	3	6	2.75–4.35	1	5.49	3.19	–	325	0.812	0.811	0.803	0.818	0.812	0.018	1.289
3	Samsung	ICR 18650 26F	2600	2450.7	2.6	5.2	2.75–4.2	1	5.40	2.85	–	362	0.857	0.855	0.841	0.648	0.858	0.010	1.148
4	Samsung	ICR 18650 22P	2200	2062.5	2.15	10	2.75–4.2	2	5.39	2.81	–	326	0.900	0.887	0.872	0.558	0.900	0.019	1.125
5	Samsung	INR 18650 35E[d]	3500	3328.6	2	13	2.65–4.2	2	5.44	3.12	–	367	0.884	0.872	0.852	0.566	0.884	0.016	1.174
6	LG	INR 18650 MJ1	3500	3021.6	3.4	10	2.5–4.2	1	4.91	3.36	–	367	0.867	0.860	0.841	0.577	0.867	0.011	1.135
7	Samsung	INR 18650 30Q	3000	2896.2	3	15	2.5–4.2	3	5.40	3.11	5.33	243	0.894	0.883	0.865	0.573	0.896	0.018	1.122
8	Samsung	INR 18650 25R	2500	2383.8	4	20	2.5–4.2	3	5.28	3.07	5.29	254	0.885	0.868	0.855	0.474	0.886	0.014	1.139
9	Samsung	INR 18650 29E	2900	2731.3	2.75	10	2.75–4.2	2	5.35	2.85	–	312	0.900	0.885	0.865	0.475	0.901	0.015	1.126
10	Samsung	INR 18650 15 L	1500	1507.2	1.45	18	2.5–4.2	1	5.35	3.10	–	299	0.841	0.837	0.821	0.722	0.841	0.023	1.198
11	Samsung	ICR 18650 22F	2250	2202.1	2.2	4.4	2.75–4.2	1	5.38	2.75	–	340	0.811	0.810	0.797	0.733	0.811	0.014	1.285
12	Samsung	ICR 18650 26H	2600	2610.2	2.6	5.2	2.75–4.2	1	5.30	2.73	–	334	0.883	0.882	0.875	0.720	0.883	0.011	1.117
13	Samsung	ICR 18650 30B	3000	2751.9	3	6	2.75–4.35	1	5.44	2.82	–	311	0.863	0.862	0.858	0.843	0.863	0.020	1.143
14	Samsung	ICR 18650 28 A	2800	2659.3	2.8	5.6	2.75–4.3	1	5.41	3.18	–	342	0.847	0.845	0.833	0.797	0.847	0.016	1.181
15	Sanyo/Panasonic	NCR 18650 GA	3500	3371.3	1.635	10	2.5–4.2	2	5.25	3.77	–	370	0.871	0.848	0.837	0.471	0.871	0.017	1.179
16	Panasonic	NCR 18650	2900	2797	1.925	5.8	2.5–4.2	2	5.10	2.50	–	322	0.838	0.833	0.820	0.741	0.838	0.025	1.232
17	Panasonic	NCR 18650 PF	2900	2812.7	2.030	10	2.5–4.2	2	5.03	2.40	–	328	0.847	0.840	0.826	0.759	0.847	0.028	1.212
18	Panasonic	NCR 18650 A	3100	2987.9	1.475	5.9	2.5–4.2	2	5.17	2.54	–	420	0.846	0.836	0.816	0.625	0.846	0.017	1.232
19	Sanyo/Panasonic	NCR 18650 BF	3350	3249.2	1.625	4.875	2.5–4.2	2	5.37	3.88	–	404	0.858	0.838	0.826	0.542	0.858	0.022	1.217
20	Sanyo/Panasonic	UR 18650 NSX	2600	2487.5	1.7	20	2.5–4.2	3	5.38	3.86	5.48	226	0.894	0.876	0.861	0.515	0.894	0.017	1.159
21	Sanyo	UR 18650 FM	2600	2370.3	1.75	5	2.5–4.2	2	5.33	3.51	–	352	0.834	0.826	0.815	0.682	0.832	0.035	1.284
22	Sanyo	NCR 18650 BL	3350	3136.6	1.62	7	2.5–4.2	2	5.34	3.87	–	397	0.837	0.813	0.799	0.386	0.838	0.015	1.312
23	LG	ICR 18650 HE2	2500	2174.6	4	20	2.5–4.2	3	5.52	3.36	5.16	228	0.875	0.851	0.841	0.410	0.876	0.018	1.172
24	LG	ICR 18650 HE4	2500	2287.5	4	20	2.5–4.2	3	5.60	3.41	5.17	245	0.877	0.861	0.846	0.627	0.878	0.033	1.152
25	LG	INR 18650 MH1	3200	3022.6	3.1	10	2.5–4.2	1	4.96	3.35	–	343	0.875	0.871	0.860	0.748	0.875	0.014	1.126
26	LG	INR 18650 HB6	1500	1253.2	4	30	2.0–4.2	3	5.48	3.28	5.10	272	0.754	0.740	0.734	0.549	0.757	0.025	1.479
27	LG	ICR 18650 HB2	1500	1407.6	4	30	2.5–4.2	3	5.49	3.38	5.20	265	0.743	0.729	0.724	0.529	0.745	0.022	1.511
28	LG	ICR 18650 S3	2200	2205	2.15	3.225	2.75–4.2	1	4.90	3.31	–	391	0.895	0.865	0.817	0.512	0.895	0.025	1.144
29	LG	ICR 18650 HD2 C	2000	2109.8	4	25	2.5–4.2	3	5.61	3.33	5.17	239	0.890	0.871	0.854	0.533	0.890	0.023	1.151
30	Sony	US 18650 VTC5	2600	2612.3	4	30	2.0–4.2	3	5.68	3.29	5.68	271	0.865	0.857	0.844	0.677	0.865	0.019	1.175
31	Samsung	ICR 18650 26H	2200	2237	1.1	2.2	3.0–4.2	1	5.42	3,14		345	0.782	0.777	0.764	0.670	0.782	0.011	1.445
32	Panasonic	NCR 18650B	3400	3202	1.7	6.8	2.5–4.2	2	5.23	2.57		413	0.872	0.862	0.841	0.571	0.872	0.014	1.267
33	Samsung	ICR 18650 26F	2600	2467.6	1.3	2.6	3.0–4.2	1	5.49	3.17		345	0.872	0.870	0.859	0.785	0.872	0.017	1.199
34	A123	APR 18650M–A1	1100	1014	5	20	2.0–3.6	4	0.62	0.55		305	0.690	0.680	0.665	0.592	0.690	0.016	1.590

[a] Maximum recommended current from the manufacturer. Note: applied charge/discharge current was 0.4 A (CCCV). [b] Thickness of full stack (copper foil – negative electrode – separator – positive electrode – aluminum – positive electrode – separator – negative electrode). [c] The graphite excess was estimated using observed cell capacity (column 5) and "mean" lithium concentration in the anode (column 15). [d] Spatially-resolved neutron diffraction data were collected at SALSA diffractometer.

© 2020 The Authors. Batteries & Supercaps published by Wiley-VCH GmbH

during full cell rotation over 360°, corresponding to an angular step of 0.36° between two projections. A single projection was averaged over three single exposures of 2000 ms each. Data reconstruction was performed using phoenix datos|x software. The analysis of the reconstructed stacks was carried out using ImageJ.[43]

Spatially resolved neutron diffraction: experimental setup

Spatially-resolved neutron powder diffraction data on the selected Li-ion batteries were collected at the materials science diffractometer STRESS-SPEC[44] at the research reactor FRM II (Heinz Maier-Leibnitz Zentrum, Garching, Germany) and the engineering diffractometer SALSA[45] (Institut Laue- Langevin, Grenoble, France). For the spatially – resolved neutron diffraction experiments, the diffraction signal was collected from the scattering ("gauge") volume defined by neutron optics, where the dimension of the volume is typically much smaller than the size of the studied object. By moving the sample different regions can be irradiated and finally a spatially resolved distribution of structural properties can be reconstructed. A photo and a sketch of the utilized experimental setup is shown in Figure 1a–b, where the incoming, diffracted and transmitted neutron beams, which define the gauge volume, are depicted. The monochromatic neutron beam with a wavelength of $\lambda \approx 1.6$ Å is limited to 2 mm in width and 17 mm in height in front of the sample using a slit system. In all cases, the data collection was performed at the center part of the battery in a plane perpendicular to its cylinder axis. The active volume of the studied cells can be approximated by two concentric cylinders, where the first one corresponds to the cell housing and the second one to the center pin. All relevant battery components like electrode coating materials, current collectors and separators are approximated to form an isotropic medium delivering a diffraction signal at a desired angle 2θ. A radial collimator with an acceptance width of 2 mm selects the scattered signal and defines the horizontal cross section of the gauge volume. The achieved distribution of the gauge volumes (points at which diffraction patterns were collected) is depicted in Figure 1b. A 2D position sensitive neutron detector (^{3}He multiwire proportional chamber) with an active area of 256×256 mm^2 was used for data collection at a sample-to-detector distance of 1056 mm located at a central scattering angle of 26 deg 2θ. The exposure times per diffraction pattern (per gauge volume) were varied within several minutes depending on the depth of the gauge volume location. After data corrections for detector nonlinearities, geometrical aberrations and curvature of diffraction rings, the data was integrated into normal 1D diffraction patterns (intensity vs. 2θ angle, Figure 1c). The utilized experimental setup was very similar at STRESS-SPEC and SALSA. The only difference was: for positioning of the cell with respect to the incoming and the diffracted beam, linear and rotational stages were used at STRESS-SPEC, whereas at SALSA a hexapod (Stewart platform) was utilized. An effectively smaller gauge volume was achieved at SALSA due to a radial oscillating collimator with 1 mm horizontal field-of-view. The detector at STRESS-SPEC had higher $2\theta \times \nu$ coverage (256×256 mm^2) compared to SALSA (80×80 mm^2).

Spatially resolved neutron diffraction: data evaluation

The central angle of the flat detector at $2\theta = 26°$ had been chosen to collect the evolution of the diffraction signal from two lithiated carbons – stage I (LiC_6) and stage II (LiC_{12}), where corresponding 001 and 002 reflections are typically present in charged batteries. Crystal structure of stage I and stage II responds weakly on lithiation[46] so that their structure factors and cell volumes can be assumed SOC independent. The relative fraction of the two phases can be used to determine the lithiation × in Li_xC_6, which has been found extremely sensitive to state-of-charge, state-of-health and temperature and, thus, is often used for monitoring the cell performance.[15–17,25,47] The 001 and 002 reflections for LiC_6 and LiC_{12} are well separated in 2θ, characterized by high intensity and are well suited for the calculation of the relative phases of stage I/stage II. Molar quantities were calculated as $n = I_{hkl}\left[V/F_{hkl}^2\right][\rho/M]$, where I_{hkl} represents the observed intensity of the Bragg reflection with Miller indices *hkl*, F_{hkl} is the corresponding structure factor, V is the unit cell volume, M is the molar mass and ρ corresponds to the density. The molar phase ratio $y = n_{LiC_6}/\left(n_{LiC_6} + n_{LiC_{12}}\right)$ can be transformed to a relative lithium concentration × of the lithiated graphite anode Li_xC_6 with $x = 1/(2-y)$. Thus × yields 1 for pure stage I with $y = 1$ and $x = 0.5$ for pure stage II and it can be used as a measure for the SOC. Typically the 001 reflection for LiC_6 vanishes at SOC < 50 %, so that × in Li_xC_6 cannot be unambiguously determined. For the current study of cells in fully charged state at least traces of the LiC_6 001 reflection were present throughout all collected datasets. No signal from low lithiated graphites ($LiC_{x>12}$) were noticed for the studied cell series with the given instrumental peak and spatial resolution.

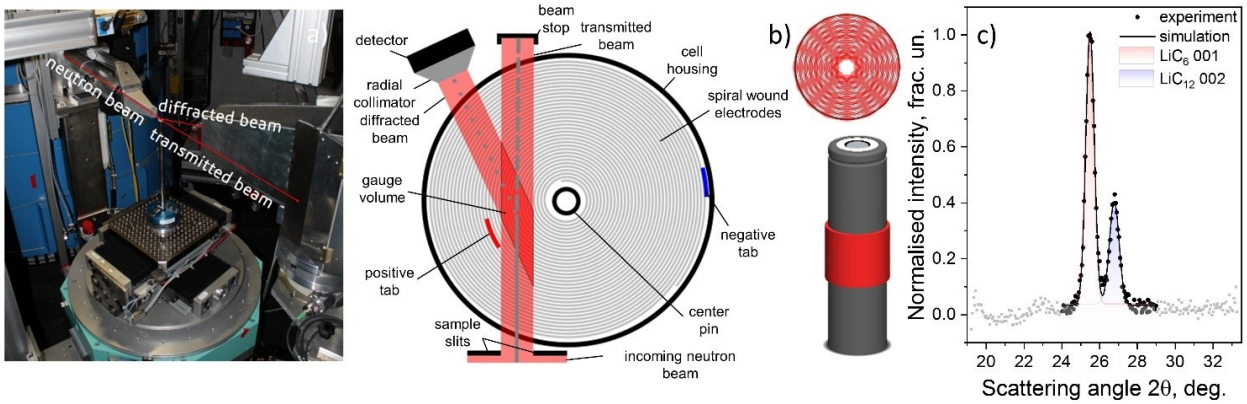

Figure 1. Photo of experimental setup (a); scheme of neutron flight path of incoming, diffracted and transmitted beam in the spatially-resolved diffraction experiment (b) along with the sketch of studied gauge volumes and the scanned area; example diffraction pattern taken from the gauge volume showing LiC_6 001 and LiC_{12} 002 reflections (c).

© 2020 The Authors. Batteries & Supercaps published by Wiley-VCH GmbH

2. Results and Discussion

Relevant cell parameters are listed in Table 1. In the current study the cells were cycled at 400 mA, which is much smaller than the nominal charge/discharge current recommended by the cell manufacturers. Nevertheless, despite the relatively "mild" cycling conditions, the obtained cell capacities were generally less than the nominal capacities specified by the cell manufacturers by 5% in average. No clear correlation between capacity differences and other cell parameters could be found on first glance.

From Table 1 it can be seen that the cell capacity displays a complex correlation character to the voltage window, charge/discharge currents, thickness of electrodes, etc. The correlations can hardly be drawn by direct comparison, but become evident when the electrical transport in the cells is included into consideration. As mentioned in Ref. [14], the current tabs/lids play a crucial role for the cycling performance of the battery. The position of the electrical connection to positive and negative current collectors defines the shape of the current distribution along the electrode stripe and determines the maximum allowed cycling (discharge) current. Temperature is another factor defining the magnitude of the current: the area where a current tab is electrically connected to a current collector becomes significantly heated due to resistive current losses (Joule heating), in comparison to the rest of the cell. Therefore, applications of extensively high discharge currents can hardly be achieved using a single current tab at the negative current collector and, therefore, two or more current collectors are often required on the anode side. It is worth to note that besides the electrode length the current density does also affect the lithium distribution over the thickness either on positive[48] or negative[49] electrodes. When no current is applied the instantaneous lithium distributions are relaxed to an intermediate lithium concentration, where time constants depend on the applied current density.[50]

The tab configurations were extracted non-destructively using X-ray microCT, where the number of current tabs, their dimensions and positions in the stack were determined. Four connection schemes were observed utilizing either two – or three – tab connections to the current collectors[1]. In cells with three-tab connections two negative ("−") current tabs to the anode were present against one positive ("+") current tab at the cathode. In all studied cells at least one "− " current tab was contacted at the outer end of anode stripe and to the cell housing. In cells adopting three-tabs another "− " current tab was placed at the opposite end of the anode stripe and the "+ " current tab was located at the middle of the electrode stripe (Scheme 3). In the two-tab schemes the "+" tab was observed either at the center pin connecting the cathode stripe at its opposite (inner) end (Scheme 1) or at the middle of the stripe (Scheme 2). As mentioned in Ref. [14], the connection of the electrode stripes via Scheme 1 usually produces a more uniform current distribution than Scheme 2 with the current supply at the middle. Interestingly, no preferences to one or another connection scheme was noticed (Scheme 2 was realized in 11 out of 34 cells; Scheme 1 in 12 out 34). Cell 34, a high power $LiFePO_4$-based cell from A123, is characterized by a unique connection configuration (Scheme 4), where the positive and the negative current tabs both are connected in the middle of the positive and the negative current collectors/electrodes[2] leading to a configuration potentially providing the lowest internal resistance.

The surface uniformity is affected by the current tabs. Besides the number and the position of the current tabs, their length is another crucial parameter defining the maximum current flow and the out-of-plane (vertical) uniformity of a 18650-type cell. Analysis of the current tab dimensions yielded a few empirical relationships:

- Cells suited for nominal discharge current above 15 A have two current tabs at the negative electrode;
- Length of "positive" current tab is linearly proportional to the applied currents;
- All studied cells can be split into four groups adopting a specific relationship between the length of the positive and the negative current tabs.

Indeed, X-Ray microCT revealed, that current tabs at the positive electrode have a length typically varying from 4.90 to 5.68 mm. In general, current tabs at the negative electrode (either single or double) are shorter[3] and their length is proportional to the ones at the opposite electrode (see Figure S1–S2). The analysis of length ratios of the current tabs displays several discrete values, which are characteristic to the cell manufacturer and the number of current collectors in the cell. There is a certain relationship between the cell capacity and the way how the current collectors are connected (Figure S3): in accordance with Table 1 the 18650-type cells built on Scheme 1 are suited for low power applications and are characterized by capacities in the range of 2000–3000 mAh; highest cell capacities are achieved applying Scheme 2; Schemes 3 and 4 are justified for cells in high power applications.

Another important parameter is the electrode thickness, which tunes the cell-specific C-rate capability and capacity. Thicknesses of the complete electrode stack including separator, negative and positive battery electrode coating and current collectors are listed in Table 1; thickness vs. discharge C-rate dependence is plotted in Figure S4. It can be seen that the electrode thickness in high power 18650-type cells (built either via Scheme 3 or 4) does not exceed 300 μm. For cells with electrodes connected via Scheme 1, the typical thickness of the electrode stack is spread from 300 to 390 μm, whereas the thickest electrode stacks (up to 420 μm) are found in cells using Scheme 2, which leads to the highest cell capacities.

The lithium concentrations obtained by spatially-resolved neutron powder diffraction are depicted in Figure 2 by false colors for all studied 18650-type cells. All data were collected at

[1] Ten out of 34 studied cells had three current tabs.

[2] Current tabs utilized in Scheme 4 are short and, therefore, not visible in the collected diffraction data of the middle of the cell height.

[3] Except cell 20, where the current tab at the negative collector has been found longer and cells 8 and 30 exhibiting nearly equally long current tabs at positive and negative current collectors.

© 2020 The Authors. Batteries & Supercaps published by Wiley-VCH GmbH

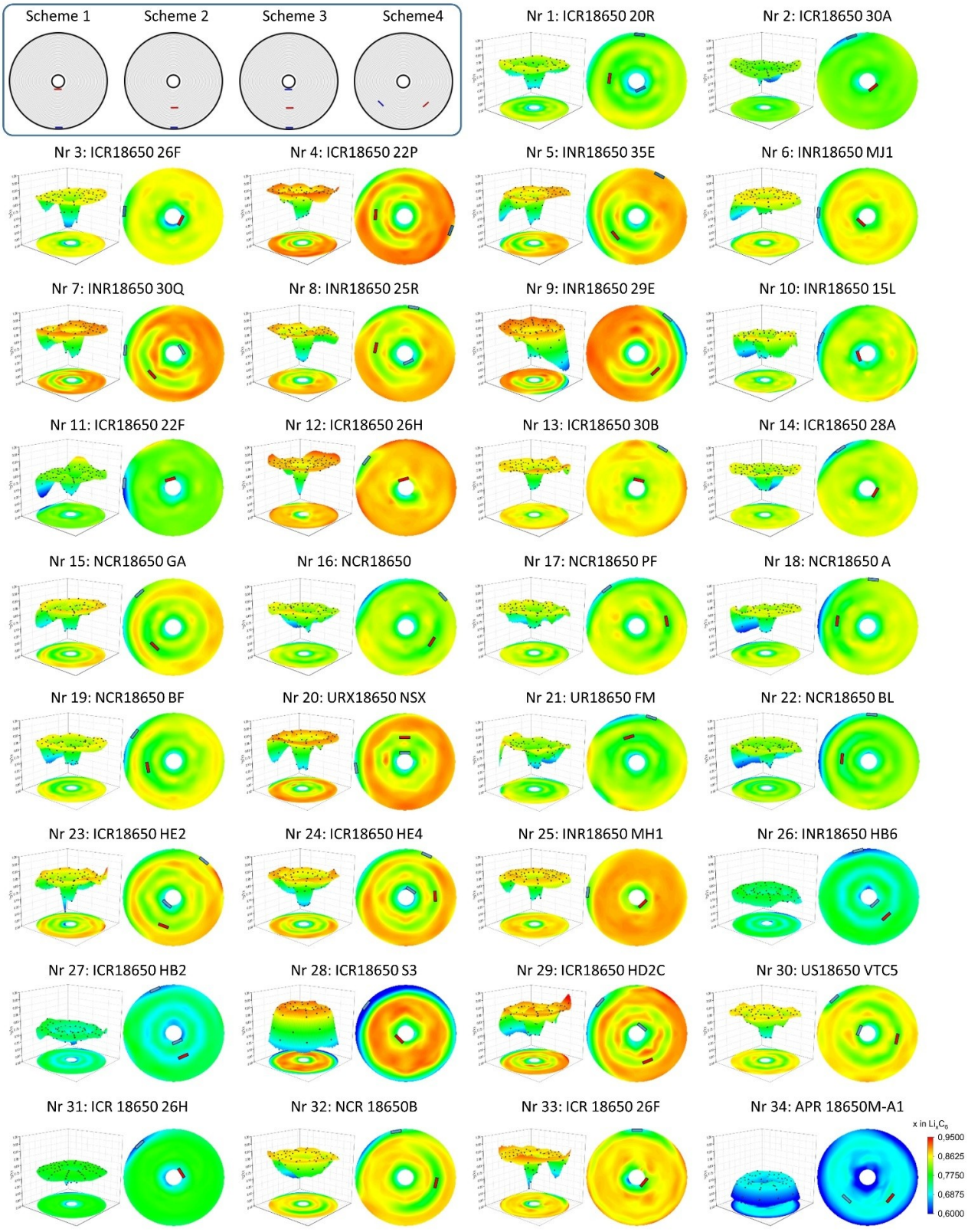

Figure 2. Lithium concentration in the graphite anode of different 18650-type cells. Data were taken at middle height. Lithium concentrations are presented by false colors, color scheme and scales are chosen to be the same for all cells. Negative and positive current tabs are presented by the black bars inside the concentration plots; blue and red colors correspond to anode and cathode current tabs. Schematic representation of electrode connections according to Schemes 1–4 is represented at the upper left corner.

© 2020 The Authors. Batteries & Supercaps published by Wiley-VCH GmbH

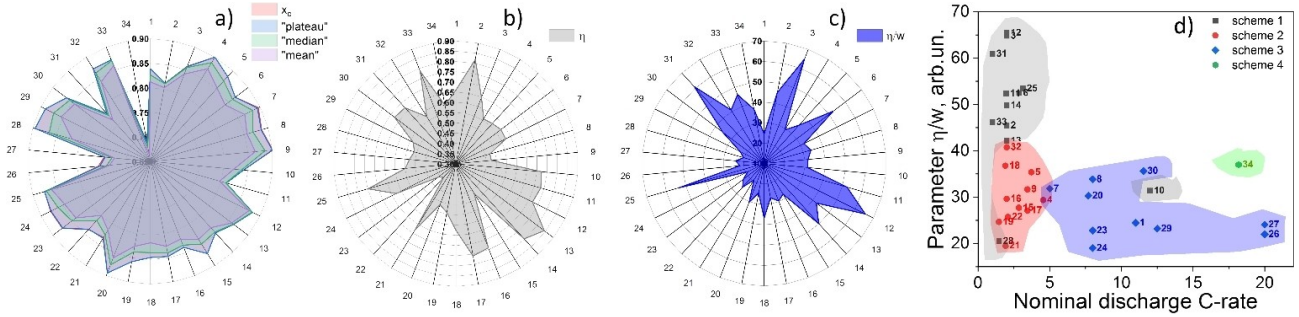

Figure 3. Spider chart diagrams of statistical parameters defining the lithium distribution (a), amount of the constant concentration plateau in the distribution histogram (Figure S5) (b), distribution of a plateau-quality parameter η/w over the studied 18650-type cells (c) and its correlation to discharge C-rate and electrode connection Schemes 1–4 (d).

the center height of the 18650-type cell. The anode and the cathode current tabs, obtained from X-ray CT, are depicted by black bars in the concentration plots with blue and red marks (corresponding to negative and positive electrodes) in the cell schematics. The obtained 2D distributions of lithiation levels have been found very different in shape and magnitude. The studied cells are suited for different applications and therefore adopt different cell chemistries and are specified for a variety of cycling currents. Different cell balancing along with an individual initial capacity loss during cell formation leads to a non-trivial correlation between cell capacity and lithiation of the anode[4].

Each cell displays its unique lithium distribution, which is characterized by a certain degree of heterogeneity, nevertheless several systematic observations can be listed:

(I) at places, where current tabs are attached to electrodes, clearly reduced graphite lithiation is observed, which can be attributed to a lack of electrode coating at these positions. Similar regions occur at the beginning and the end of each electrode stripe due to missing electrode coatings.[32]

(II) cells with electrode connections according to Scheme 1 and 2 display the most uniform lithium distribution—characterized by a clearly defined 2D plateau behavior;

(III) lithium non-uniformities at the center of the electrode stripes are observed for cells with electrode connection of Scheme 2 and 3, where the area of the observed non-uniformities was quite different.

Observation (III) is to a large extent affected by the spatial resolution of the experimental setup. Nevertheless, the presence of rather "narrow" non-uniformities in the middle of the electrode roll of cells 4–5 to highly non-uniform cases (ring shaped) as in cells 15, 19, 26 or 27, point to the real character of heterogeneous distribution in these cells. Furthermore, statement (I) has to be extended by considering the temperature: near the current tabs the highest current density and, correspondingly, the highest temperature is supposed to occur being a potential reason for non-uniformity.

A more detailed analysis of the 2D lithium distributions presented in Figure 2 requires quantitative indicators capable to characterize the properties of the distribution, its uniformity and conformity. In Ref. [32], several statistical parameters were proposed to characterize the observed 2D distribution, namely the mean value and its standard deviation describing the average lithium concentration $<x_{Li}>$, the median of the distribution and the plateau value x_p. As recently shown, these statistic indicators perform well for a set of variously aged cells belonging to a common cell type and the same batch. However, practice shows that "mean", "median" and "plateau" parameters obtained for different cell types cannot be correlated directly to other cell properties listed in Table 1 due to different chemistries, balancing and irreversible capacity loss upon cell formation. A direct comparison, consequently, requires a more generalized approach. For example, instead of using integral statistical parameters, the uniformity of the distribution can adequately be quantified by the analysis of distribution histograms. The histograms of the lithium distributions displayed in Figure 2 are shown in Figure S5. Their shape is significantly different from a δ-function expected for an ideal uniform system[5]. Instead of that it can be represented by a main peak corresponding to the constant lithiation plateau and a broad hump caused by non-uniformity. The plateau peak was fitted with a gaussian to obtain the estimate for × in Li_xC_6 for the plateau value corresponding to the peak position x_c, and the homogeneity of the plateau – width of the peak w. Degree of homogeneity corresponding to the amount of plateau area in the whole histogram was calculated as $\eta = A_p/A_c$, where A_p is the integral intensity of the gauss fit and $A_c = \int histogram$ is the integral over the whole histogram.

The x_c parameters were obtained for each cell (see Table 1) and are plotted in Figure 3a together with "mean" and "median" indicators in the form of a "spider" chart. All three indicators are very close with the best agreement between x_c and the "median" values. Besides x_c and w describing the constant concentration plateau and its "width", the integral uniformity parameter η was estimated for each cell and are plotted in Figure 3b. A list of cells (Nr. 13, 2, 14, 33, 17) is yield where a uniform plateau-like behavior is dominating. Accord-

[4] Excess of carbon used for cell balancing purposes was determined on the basis of observed cell capacities and experimental lithium concentrations in the graphite and is listed for each cell in Table 1 (column 20).

[5] An isotropic lithiation level × in Li_xC_6 for the entire anode is expected to reach an equilibrium state after charging with extended CV with low current cut-off values, e.g., $I_c < Q/100$ or less

© 2020 The Authors. Batteries & Supercaps published by Wiley-VCH GmbH

ingly, evaluation of "1-η" (Figure S6a) creates a list of cells with the most heterogeneous lithiation levels (22, 23, 15, 8, 9), where no obvious correlation to cell capacity, nominal discharge current, electrode thickness etc. (Figure S6) can be established.

Even in cells with a dominant plateau region the lithiation plateau is often not ideally flat (constant), i.e. its perfectness is determined by the width w_1 (Figure S6c) defining its deviation from the constant. Again, several cells with relatively high w can be identified (Nr. 21, 24, 17, 1, 16) along with the list of cells (3, 6, 12, 31, 25) where deviations of the plateau values are minimal. Based on this, a plateau-quality parameter η/w (Figure 3c) can be proposed[6], which is an area fraction of the plateau with respect to its "width". The best plateau-quality parameters were observed for cells 12, 3, 31, 6, 25.

A closer look on the cell properties revealed a clear correlation between plateau-quality parameter, location of the lids and discharge current (Figure 3d). Although the rather qualitative fitting approach, the results in general have been found in good agreement with Figure 2. One can notice that cells built according to Scheme 1 are characterized by the best defined plateau of constant lithium concentration. Electrode connection schemes 2–4 generally lead to a more heterogeneous behavior resulting in a non-uniform spread and less pronounced concentration plateaus, which might be an intentional compromise maintaining internal cell resistance low.

3. Conclusions

A number of 34 Li-ion cells of 18650-type from different manufacturers was studied. The chosen cells were based on different cell chemistries and were designed for different applications, charge currents, protocols and voltage windows. Common features of the studied cells are their cylinder type shape, rolled electrode stacks and graphite anode, which were the factors defining the cell selection. The distribution of lithium in the graphite anode for the set of Li-ion batteries was probed using a combination of spatially-resolved neutron diffraction, X-ray computed tomography and electrochemistry. Studies were performed in fully charged state using low cycling currents and CCCV charging protocol with small cut-off[7].

All studies were performed non-destructively. The cell layout: thickness of electrode stacks and details of its winding, position, length and the number of current tabs, center pins, gas vent and electric contacts were determined for each cell. Correlations between the number, length and position of current tabs, thickness of electrode stack, cell capacity and nominal cycling currents (C-rates) were established.

The 2D lithium distribution $\times$ in Li_xC_6 was extracted from diffraction intensities at the middle height of each cell. The location of the current tabs and their connection to the electrode stripes have been found correlated to the lithium distribution inside the graphite anode. Four commonly used schemes of the current lid connection were identified, where cells with an electrode connection in line with Scheme 1 display the most uniform lithiation; electrode connections via schemes 2 and 3 lead to lithium non-uniformities at the center of the electrode stripes: the cell build on Scheme 4 is characterized by the largest non-uniformity with a very narrow concentration plateau and a vertical gradient of lithium concentrations.[14]

The performed experiments suffered from the limited spatial resolution of the experimental setup for neutron diffraction, i.e. it would be highly desirable to improve spatial resolution down to μm or even sub μm range. A straightforward approach using the same experimental geometry along with a drastic reduction of the gauge volume would lead to scattering signals below the detection limit. Therefore, new strategies and methodologies of data collection, capable to add depth resolution to the diffraction data, are highly desired, e.g. synchrotron radiation using small focused beams or developing a data collection strategy enabling inverse Radon transforms and so on.

In summary: lithium uniformity depends on different factors such as spatial current distribution, electrode morphology, electrolyte distribution and wetting, state and type of solid-electrolyte interphase, different kinds of geometrical boundary conditions *etc.*. Nature and origin of the underlying processes defining lithium distribution inside the anode are highly relevant for building safe, stable and high-performance next generation Li-ion cells. The current tabs inside the electrode rolls have been found to positively affect the cycling performance (C-rates), but cause irregularities in the electrode coating. This along with incomplete coating of the electrodes at both ends effects the shape of lithium distribution and define the islands of heterogeneity limiting the local lithium exchange.

Acknowledgements

The authors acknowledge the access to the research infrastructure of Heinz Maier-Leibnitz Zentrum (Germany) and Institut Laue – Langevin (France). The study was supported in part by German Ministry of Education and Science (Projects 05K16VK2 and 05K19VK3) and Heinz Maier-Leibnitz Zentrum. KA and FP acknowledge financial support through the DFG Gottfried Wilhelm Leibniz program. Assistance of Dr. W. Gan (Helmholtz Zentrum Geesthacht) and Dr. J. Rebello-Kornmeier (Technische Universität München) with spatially-resolved neutron diffraction experiments at STRESS-SPEC is gratefully acknowledged. We acknowledge DESY (Hamburg, Germany), a member of the Helmholtz Association HGF, for the provision of experimental facilities. Parts of this research were carried out at PETRA III using beamline P02.1. Open access funding enabled and organized by Projekt DEAL.

[6] Obtained distributions of dividend and divisor in η/w quality parameter (η and $1/w$) are showed vs. C-rate in Figure S7a–b along with their relationship to each other $1/w$ vs. η (Figure S7c).

[7] Use of high charging currents and cut-off values would potentially introduce even larger non-uniformities.

© 2020 The Authors. Batteries & Supercaps published by Wiley-VCH GmbH

Conflict of Interest

The authors declare no conflict of interest.

Keywords: lithiated graphite · Li-ion batteries · lithium concentration · heterogeneity · neutron diffraction

[1] B. Scrosati, J. Hassoun, Y. K. Sun, *Energy Environ. Sci.* **2011**, *4*, 3287–3295.
[2] M. Armand, J. M. Tarascon, *Nature* **2008**, *451*, 652–657.
[3] B. Diouf, R. Pode, *Renewable Energy* **2015**, *76*, 375–380.
[4] A. Barre, B. Deguilhem, S. Grolleau, M. Gerard, F. Suard, D. Riu, *J. Power Sources* **2013**, *241*, 680–689.
[5] V. Agubra, J. Fergus, *Materials* **2013**, *6*, 1310–1325.
[6] J. Vetter, P. Novak, M. R. Wagner, C. Veit, K. C. Moller, J. O. Besenhard, M. Winter, M. Wohlfahrt-Mehrens, C. Vogler, A. Hammouche, *J. Power Sources* **2005**, *147*, 269–281.
[7] D. Burow, K. Sergeeva, S. Calles, K. Schorb, A. Borger, C. Roth, P. Heitjans, *J. Power Sources* **2016**, *307*, 806–814.
[8] P. J. Osswald, S. V. Erhard, A. Rheinfeld, B. Rieger, H. E. Hoster, A. Jossen, *J. Power Sources* **2016**, *329*, 546–552.
[9] P. J. Osswald, S. V. Erhard, A. Noel, R. Keil, F. M. Kindermann, H. Hoster, A. Jossen, *J. Power Sources* **2016**, *314*, 93–101.
[10] S. V. Erhard, P. J. Osswald, P. Keil, E. Hoffer, M. Haug, A. Noel, J. Wilhelm, B. Rieger, K. Schmidt, S. Kosch, F. M. Kindermann, F. Spingler, H. Kloust, T. Thoennessen, A. Rheinfeld, A. Jossen, *J. Electrochem. Soc.* **2017**, *164*, A6324–A6333.
[11] G. S. Zhang, C. E. Shaffer, C. Y. Wang, C. D. Rahn, *J. Electrochem. Soc.* **2013**, *160*, A610–A615.
[12] G. S. Zhang, C. E. Shaffer, C. Y. Wang, C. D. Rahna, *J. Electrochem. Soc.* **2013**, *160*, A2299–A2305.
[13] J. Wilhelm, S. Seidlmayer, S. Erhard, M. Hofmann, R. Gilles, A. Jossen, *J. Electrochem. Soc.* **2018**, *165*, A1846–A1856.
[14] A. Senyshyn, M. J. Muhlbauer, O. Dolotko, M. Hofmann, H. Ehrenberg, *Sci. Rep.* **2015**, *5*, 18380.
[15] X.-L. Wang, K. An, L. Cai, Z. Feng, S. E. Nagler, C. Daniel, K. J. Rhodes, A. D. Stoica, H. D. Skorpenske, C. Liang, W. Zhang, J. Kim, Y. Qi, S. J. Harris, *Sci. Rep.* **2012**, *2*, 747.
[16] O. Dolotko, A. Senyshyn, M. J. Muhlbauer, K. Nikolowski, H. Ehrenberg, *J. Power Sources* **2014**, *255*, 197–203.
[17] O. Dolotko, A. Senyshyn, M. J. Muhlbauer, K. Nikolowski, F. Scheiba, H. Ehrenberg, *J. Electrochem. Soc.* **2012**, *159*, A2082–A2088.
[18] O. Bergstrom, A. M. Andersson, K. Edstrom, T. Gustafsson, *J. Appl. Crystallogr.* **1998**, *31*, 823–825.
[19] F. Rosciano, M. Holzapfel, W. Scheifele, P. Novak, *J. Appl. Crystallogr.* **2008**, *41*, 690–694.
[20] M. Roberts, J. J. Biendicho, S. Hull, P. Beran, T. Gustafsson, G. Svensson, K. Edstrom, *J. Power Sources* **2013**, *226*, 249–255.
[21] J. J. Biendicho, M. Roberts, C. Offer, D. Noreus, E. Widenkvist, R. I. Smith, G. Svensson, K. Edstrom, S. T. Norberg, S. G. Eriksson, S. Hull, *J. Power Sources* **2014**, *248*, 900–904.
[22] N. Paul, J. Wandt, S. Seidlmayer, S. Schebesta, M. J. Muehlbauer, O. Dolotko, H. A. Gasteiger, R. Gilles, *J. Power Sources* **2017**, *345*, 85–96.
[23] M. A. Rodriguez, M. H. Van Benthem, D. Ingersoll, S. C. Vogel, H. M. Reiche, *Powder Diffr.* **2010**, *25*, 143–148.
[24] A. Senyshyn, M. J. Muhlbauer, K. Nikolowski, T. Pirling, H. Ehrenberg, *J. Power Sources* **2012**, *203*, 126–129.
[25] A. Senyshyn, O. Dolotko, M. J. Muhlbauer, K. Nikolowski, H. Fuess, H. Ehrenberg, *J. Electrochem. Soc.* **2013**, *160*, A3198–A3205.
[26] D. Goonetilleke, N. Sharma, W. K. Pang, V. K. Peterson, R. Petibon, J. Li, J. R. Dahn, *Chem. Mater.* **2019**, *31*, 376–386.
[27] D. Sheptyakov, L. Boulet-Roblin, V. Pomjakushin, P. Borel, C. Tessier, C. Villevieille, *J. Mater. Chem. A* **2020**, *8*, 1288–1297.
[28] D. Goonetilleke, J. C. Pramudita, M. Hagan, O. K. Al Bahri, W. K. Pang, V. K. Peterson, J. Groot, H. Berg, N. Sharma, *J. Power Sources* **2017**, *343*, 446–457.
[29] S. Taminato, M. Yonemura, S. Shiotani, T. Kamiyama, S. Torii, M. Nagao, Y. Ishikawa, K. Mori, T. Fukunaga, Y. Onodera, T. Naka, M. Morishima, Y. Ukyo, D. S. Adipranoto, H. Arai, Y. Uchimoto, Z. Ogumi, K. Suzuki, M. Hirayama, R. Kanno, *Sci. Rep.* **2016**, *6*, 28843.
[30] L. Boulet-Roblin, P. Borel, D. Sheptyakov, C. Tessier, P. Novak, C. Villevieille, *J. Phys. Chem. C* **2016**, *120*, 17268–17273.
[31] L. Boulet-Roblin, D. Sheptyakov, P. Borel, C. Tessier, P. Novák, C. Villevieille, *J. Mater. Chem. A* **2017**, *5*, 25574–25582.
[32] D. Petz, M. J. Mühlbauer, V. Baran, M. Frost, A. Schökel, C. Paulmann, Y. Chen, D. Garcés, A. Senyshyn, *J. Power Sources* **2020**, *448*, 227466.
[33] M. J. Mühlbauer, D. Petz, V. Baran, O. Dolotko, M. Hofmann, R. Kostecki, A. Senyshyn, *J. Power Sources* **2020**, *475*, 228690.
[34] V. Baran, O. Dolotko, M. J. Muhlbauer, A. Senyshyn, H. Ehrenberg, *J. Electrochem. Soc.* **2018**, *165*, A1975–A1982.
[35] A. Senyshyn, M. J. Muhlbauer, O. Dolotko, H. Ehrenberg, *J. Power Sources* **2015**, *282*, 235–240.
[36] L. Cai, K. An, Z. L. Feng, C. D. Liang, S. J. Harris, *J. Power Sources* **2013**, *236*, 163–168.
[37] X. H. Yu, Z. L. Feng, Y. Ren, D. Henn, Z. G. Wu, K. An, B. Wu, C. Fau, C. Li, S. J. Harris, *J. Electrochem. Soc.* **2018**, *165*, A1578–1585.
[38] A. Senyshyn, M. J. Muhlbauer, O. Dolotko, M. Hofmann, T. Pirling, H. Ehrenberg, *J. Power Sources* **2014**, *245*, 678–683.
[39] M. J. Muhlbauer, O. Dolotko, M. Hofmann, H. Ehrenberg, A. Senyshyn, *J. Power Sources* **2017**, *348*, 145–149.
[40] S. C. Nagpure, R. G. Downing, B. Bhushan, S. S. Babu, L. Cao, *Electrochim. Acta* **2011**, *56*, 4735–4743.
[41] H. Kawaura, M. Harada, Y. Kondo, H. Kondo, Y. Suganuma, N. Takahashi, J. Sugiyama, Y. Seno, N. L. Yamada, *ACS Appl. Mater. Interfaces* **2016**, *8*, 9540–9544.
[42] T. K. Zakharchenko, M. V. Avdeev, A. V. Sergeev, A. V. Chertovich, O. I. Ivankov, V. I. Petrenko, Y. Shao-Horn, L. V. Yashina, D. M. Itkis, *Nanoscale* **2019**, *11*, 6838–6845.
[43] C. A. Schneider, W. S. Rasband, K. W. Eliceiri, *Nat. Methods* **2012**, *9*, 671–675.
[44] M. Hofmann, R. Schneider, G. A. Seidl, J. Rebelo-Kornmeier, R. C. Wimpory, U. Garbe, H. G. Brokmeier, *Phys. B* **2006**, *385–86*, 1035–1037.
[45] T. Pirling, G. Bruno, P. J. Withers, *Mater. Sci. Eng. A* **2006**, *437*, 139–144.
[46] C. Didier, W. K. Pang, Z. P. Guo, S. Schmid, V. K. Peterson, *Chem. Mater.* **2020**, *32*, 2518–2531.
[47] N. Sharma, V. K. Peterson, M. M. Elcombe, M. Avdeev, A. J. Studer, N. Blagojevic, R. Yusoff, N. Kamarulzaman, *J. Power Sources* **2010**, *195*, 8258–8266.
[48] J. Liu, M. Kunz, K. Chen, N. Tamura, T. J. Richardson, *J. Phys. Chem. Lett.* **2010**, *1*, 2120–2123.
[49] D. P. Finegan, A. Quinn, D. S. Wragg, A. M. Colclasure, X. Lu, C. Tan, T. M. M. Heenan, R. Jervis, D. J. L. Brett, S. Das, T. Gao, D. A. Cogswell, M. Z. Bazant, M. Di Michiel, S. Checchia, P. R. Shearing, K. Smith, *Energy Environ. Sci.* **2020**, *13*, 2570–2584.
[50] T. Kitamura, S. Takai, T. Yabutsuka, T. Yao, *J. Phys. Chem. Solids* **2020**, *142*, 109440.

Manuscript received: October 16, 2020
Revised manuscript received: October 26, 2020
Accepted manuscript online: October 28, 2020
Version of record online: November 23, 2020

© 2020 The Authors. Batteries & Supercaps published by Wiley-VCH GmbH